Eur. Phys. J. D **28**, 423–433 (2004)
DOI: 10.1140/epjd/e2004-00012-8

**THE EUROPEAN
PHYSICAL JOURNAL D**

3–D numerical simulation of fully-coupled particle heating in ICPTs

D. Bernardi[1], V. Colombo[1,a], E. Ghedini[1], A. Mentrelli[1], and T. Trombetti[2]

[1] Dipartimento di Ingegneria delle Costruzioni Meccaniche, Nucleari, Aeronautiche e di Metallurgia (DIEM) and Centro Interdipartimentale di Ricerca per le Applicazioni della Matematica (CIRAM), Università di Bologna, via Saragozza 8, 40123 Bologna, Italy

[2] Dipartimento di Ingegneria delle Costruzioni Meccaniche, Nucleari, Aeronautiche e di Metallurgia (DIEM), Università di Bologna, viale del Risorgimento 2, 40136 Bologna, Italy

Received 5 September 2003 / Received in final form 5 January 2004

Abstract. Numerical simulations of the trajectory and heating history of powders injected with a carrier-gas into inductively coupled plasma torches working at atmospheric pressure have been performed in the framework of a 3–D FLUENT©-based model, taking into account the effects of coupling between particles and plasma. In this paper, we present a selection of the results obtained for different operating conditions of the torch and for different characteristics of the injected particles.

PACS. 52.75.Hn Plasma torches – 52.65.-y Plasma simulation – 52.80.Pi High-frequency and RF discharges – 81.20.Ev Powder processing: powder metallurgy, compaction, sintering, mechanical alloying, and granulation

1 Introduction

Inductively coupled plasma torches (ICPTs) are successfully used as high-temperature sources in a wide range of applications, such as spheroidization and purification of both metallic and ceramic powders [1]. However, the effectiveness of these processes strongly depends on a large number of parameters, including the torch operating conditions and the type and characteristics of the injected powders. This causes the *try and fail* approach to be expensive and difficult to carry out. In this frame, numerical modelling represents a useful tool that may help in the design and optimization of these processes. Several numerical models have been developed in a recent past: 2–D axisymmetric models [2,3] for the analysis of the motion and heating history of the particle inside the torch region, as well as 3–D models to simulate thermal plasma jets with particle and carrier gas injected downstream of the torch exit [4,5]. Recently, a new 3–D FLUENT©-based model for the evaluation of the trajectory and thermal history of particles injected, by means of an injection probe, together with a carrier-gas, into ICPTs working at atmospheric pressure has been presented by the authors [6–9]. In this paper we present an exhaustive selection of the results obtained for different operating conditions of the ICPT (calculations have been performed for different discharge powers, frequencies of the RF generator, inlet gas velocity characteristics) as well as for different types and characteristics of the injected particles, taking also into account the effects of the particle injection on the plasma.

2 Mathematical model

The fully 3–D FLUENT©-based model previously developed by the authors [10] (who have also developed a 2–D model within the FLUENT© environment using different approaches for the treatment of the electromagnetic field [11]), suitably modified to keep into account the appropriate source-sink terms in the continuity, momentum and energy equations, is employed to calculate plasma temperature and velocity fields in the torch region. Continuity, momentum and energy equations are solved for optically thin Ar plasmas under the assumptions of LTE and laminar flow, while a grid extending outside the torch region is employed for the treatment of the electromagnetic field. The simplified electromagnetic model is adopted here, being the effect of the electric scalar potential due to the charge density distribution that arises in the plasma negligible, as shown in [12–14].

The computational grid is a hybrid one composed by tetrahedrons, hexahedrons and wedges, and it is built by means of the GAMBIT© software package and then imported into the FLUENT© environment. The

---

[a] e-mail: `colombo@ciram.ing.unibo.it`

approximate number of cells composing the grid is 4.5×10^5. Simulations have been carried on a cluster of workstations, i.e. splitting up the grids and data in various partitions and then assigning each partition to a different computing process.

The particles are axially injected with velocity equal to that of the carrier gas and are assumed to be spherical and with a negligible internal resistance to heat transfer. The effects of the particle injection on the plasma is suitably taken into account by adding proper exchange terms in the fluid dynamics equations, as explained in [15].

The particles trajectory is obtained by solving the following equation of motion:

$$\rho_p \frac{d\mathbf{v_p}}{dt} = \left(\frac{3\rho_\infty C_D}{4d_p}\right) |\mathbf{v}_\infty - \mathbf{v_p}| (\mathbf{v}_\infty - \mathbf{v_p}) + \mathbf{g}(\rho_p - \rho_\infty) \tag{1}$$

where $\mathbf{v}_\infty$ and ρ_∞ are the velocity and density of the plasma; $\mathbf{v_p}$, d_p, ρ_p are the velocity, diameter and density of the particle, respectively; $\mathbf{g}$ is the gravitational acceleration; C_D is the drag coefficient which is calculated as in [4] but neglecting the Knudsen (rarefaction) effect:

$$C_D = \gamma f(Re_\infty) \left(\frac{Re_\infty}{Re_w}\right)^{0.1} = \gamma f(Re_\infty) \left(\frac{\nu_\infty}{\nu_w}\right)^{0.1}. \tag{2}$$

In equation (2), ν_∞ and ν_w are the values of the gas kinematic viscosity calculated at the plasma and particle temperatures, T_∞ and T_p, respectively; $f(Re_\infty)$ is the following function of the Reynolds number $Re_\infty = d_p |\mathbf{v}_\infty| / \nu_\infty$:

$$f(Re_\infty) = \begin{cases} \dfrac{24}{Re_\infty} & Re_\infty < 0.2 \\ \left(\dfrac{24}{Re_\infty}\right)(1 + 0.1875 Re_\infty) & 0.2 \le Re_\infty < 2 \\ \left(\dfrac{24}{Re_\infty}\right)\left(1 + 0.11 Re_\infty^{0.81}\right) & 2 \le Re_\infty < 21 \\ \left(\dfrac{24}{Re_\infty}\right)\left(1 + 0.189 Re_\infty^{0.632}\right) & 21 \le Re_\infty < 200 \end{cases} \tag{3}$$

and γ is a correction factor accounting for the effect due to the particle evaporation (if it occurs):

$$\gamma = \frac{\lambda_v}{S_\infty - S_w} \int_{T_w}^{T_\infty} \frac{k_\infty}{h_\infty - h_w + \lambda_v} dT \tag{4}$$

where λ_v is the latent heat of evaporation of the particle material, h_∞, h_w are the values of the gas specific enthalpy evaluated at the plasma and particle temperatures, respectively, k_∞ is the plasma thermal conductivity and S_∞, S_w are the heat conduction potentials calculated at T_∞ and T_p, following the definition of $S(T)$:

$$S(T) = \int_{T_0}^{T} k(T) dT \tag{5}$$

being T_0 an arbitrary reference temperature. The heating history of the particle in the solid-phase is obtained by solving the energy balance equation:

$$m_p c_p \frac{dT_p}{dt} = A_p h_c (T_\infty - T_p) - A_p \epsilon \sigma \left(T_p^4 - T_a^4\right) \tag{6}$$

where m_p and A_p are the mass and the surface area of the particle; c_p and ϵ are the specific heat and the emissivity of the particle material; σ is the Stefan–Boltzmann constant (5.67×10^{-8} W/m^2 K^4); T_a is the room temperature (300 K) and h_c is the convective coefficient given by:

$$h_c = \gamma \frac{Nu (S_\infty - S_w)}{d_p (T_\infty - T_p)} \tag{7}$$

where Nu is the Nusselt number calculated as in [4]:

$$Nu = 2 \left[1 + 0.63 Re_\infty Pr_\infty^{0.8} \left(\frac{Pr_w}{Pr_\infty}\right)^{0.42} \times \left(\frac{\rho_\infty \mu_\infty}{\rho_w \mu_w}\right)^{0.52} C^2\right]^{0.5} \tag{8}$$

where ρ_∞, μ_∞, Pr_∞ are the density, the dynamic viscosity and the Prandtl number ($Pr = \mu c_p / k$) of the gas, respectively, evaluated at the plasma temperature; ρ_w, μ_w, Pr_w are the same quantities calculated at the particle temperature, while C is a factor whose expression is:

$$C = \frac{1 - \left(\frac{h_w}{h_\infty}\right)^{1.14}}{1 - \left(\frac{h_w}{h_\infty}\right)^{2}}. \tag{9}$$

As soon as the particle temperature reaches the melting point, it is assumed to remain constant and the liquid-phase fraction, x, is calculated by integrating the equation:

$$\frac{dx}{dt} = \frac{6q}{\rho_p d_p \lambda_m} \tag{10}$$

where q is the net specific heat flux transferred to the particle, given by the right-hand side of equation (6), and λ_m is the melting latent heat of the particle material. Once the particle is completely melted ($x = 1$), its temperature is allowed to follow again equation (6). As soon as the evaporation point is achieved, the temperature of the particle is kept constant while its diameter reduces itself according to the following law:

$$\frac{dd_p}{dt} = -\frac{2q}{\rho_p \lambda_v}. \tag{11}$$

It is worth noting that, in the present model, no mass transfer between particles and plasma is accounted for; i.e. the eventual evaporated fraction of the particles does not alter the composition of the surrounding plasma gas, which is considered to be always pure argon.

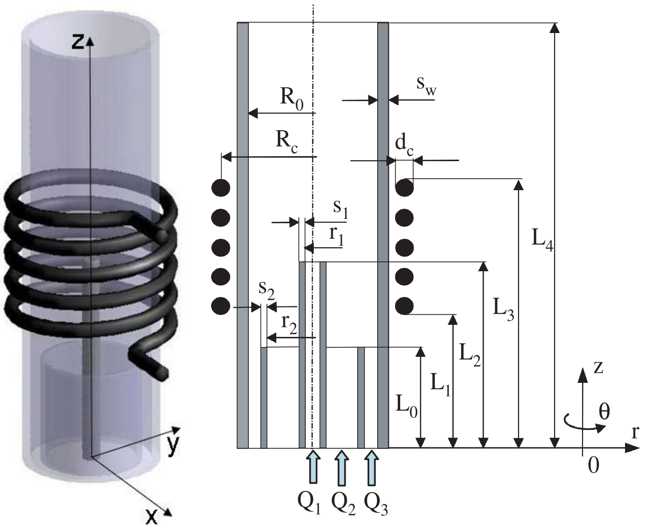

Fig. 1. 3–D schematic of the inductively coupled plasma torch.

Table 1. Dimensions and operating conditions of the inductively coupled plasma torch sketched in Figure 1.

$r_1 = 1.7$ mm	$L_0 = 40$ mm
$r_2 = 19$ mm	$L_1 = 50$ mm
$R_0 = 25$ mm	$L_2 = 80$ mm
$R_c = 33$ mm	$L_3 = 110$ mm
$d_c = 6$ mm	$L_4 = 170$ mm
$s_1 = 2$ mm	$Q_1 = 5$ slpm
$r_2 = 2.2$ mm	$Q_2 = 30$ slpm
$s_w = 3.5$ mm	$Q_3 = 120$ slpm
Particles are injected in the discharge at $z_{inj} = L_2$	

3 Selected numerical results

Calculations have been performed for different RF generator frequencies f (3 MHz and 5 MHz), net power dissipated in the discharge P (15 kW and 25 kW) and inlet gas velocity distributions (with or without swirl component in the plasma and sheath gases, $v_{\theta p}$ and $v_{\theta s}$, respectively), as well as for various materials (Ni, Al_2O_3, W) and diameters (ranging from 30 μm to 100 μm) of the injected particles. Torch dimensions and operating conditions adopted in the calculations are reported in Figure 1 and Table 1. All particles are assumed to be axially injected in the discharge, with total mass feed rate equal to 20 g/min, from 38 different streams starting from the centroids (located on the horizontal plane at (x_{inj}, y_{inj}), with $(x_{inj}^2 + y_{inj}^2)^{1/2} < r_1$) of the grid faces that discretize the exit section of the injection probe at $z_{inj} = 80$ mm (see Figs. 1 and 2). In Figure 2, the injection points with the numbered black dots will be referred to in this section as starting points for trajectories and heating histories of the injected particles. Initial surface temperature for all the injected particles is set to 300 K. Physical properties of the injected particles are summarized in Table 2.

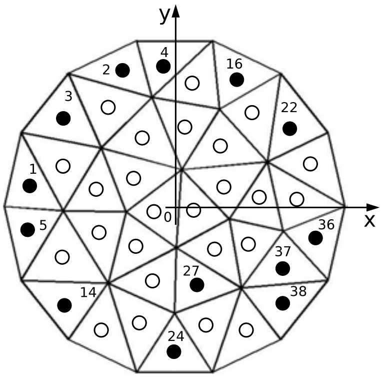

Fig. 2. Schematic of the exit section of the injection probe with its discretizing grid and carrier gas and particles injection points.

Table 2. Physical properties of the injected particles.

Physical property	Al_2O_3	Ni	W
Density, ρ_p [kg/m^3]	3900	8906	19250
Melting point, T_m [K]	2326	1726	3695
Boiling point, T_b [K]	3800	3187	5930
Latent heat of melting, λ_m [kJ/kg]	1065	298	190
Latent heat of boiling, λ_b [kJ/kg]	25000	620	4346
Specific heat of solid, $c_{p,s}$ [kJ/kgK]	as in [16]	as in [17]	0.132
Specific heat of liquid, $c_{p,l}$ [kJ/kgK]	1.2	0.734	0.132
Emissivity of solid, ϵ_s [–]	0.3	0.3	0.38
Emissivity of liquid, ϵ_l [–]	0.9	0.3	0.38

Table 3. Torch operating conditions and particle materials for the various cases under study.

CASE	P [kW]	f [MHz]	$v_{\theta p}$ [m/s]	$v_{\theta s}$ [m/s]	particle material
A	25	3	-	-	Al_2O_3
B	25	3	-	-	Ni
C	25	3	20	-	Ni
D	25	3	-	20	Ni
E	25	5	-	20	Ni
F	15	3	-	10	Al_2O_3
G	15	3	-	10	Ni
H	25	3	-	-	W

Eight reference cases (`CASE A` – `CASE H`) characterized by different torch operating conditions and particle materials have been considered (see Tab. 3). For the sake of conciseness, three-dimensional plasma temperature and velocity fields for each of these cases with no particle feeding are not reported here; 3–D reference results for the same torch operating conditions but with carrier gas flow rate $Q_1 = 10$ slpm have already been presented in [13,14].

The following choice has been made for what concerns the presentation of our results. All the figures showing results in terms of particle temperature, T_p, and particle velocity, v_p, as function of time (from particle injection time, $t = 0$, to the time corresponding to particle reaching the exit of the torch) will refer to one particular injection

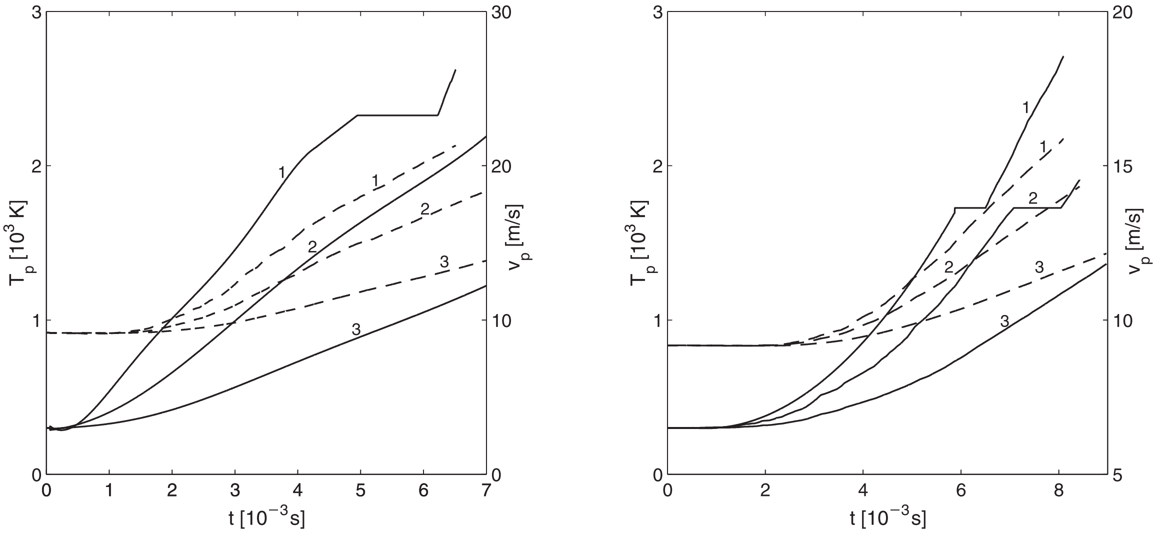

(a) (b)

Fig. 3. Temperature (—) and velocity (- -) of the particles as function of time for (a) `CASE A` (Al_2O_3 particles with $d_{p1,2,3} = 30$, 50, 100 μm and injection point: $x_{inj} = -1.1$ mm, $y_{inj} = -0.9$ mm); (b) `CASE B` (Ni particles with $d_{p1,2,3} = 30$, 50, 100 μm and injection point: $x_{inj} = 0.2$ mm, $y_{inj} = -0.8$ mm).

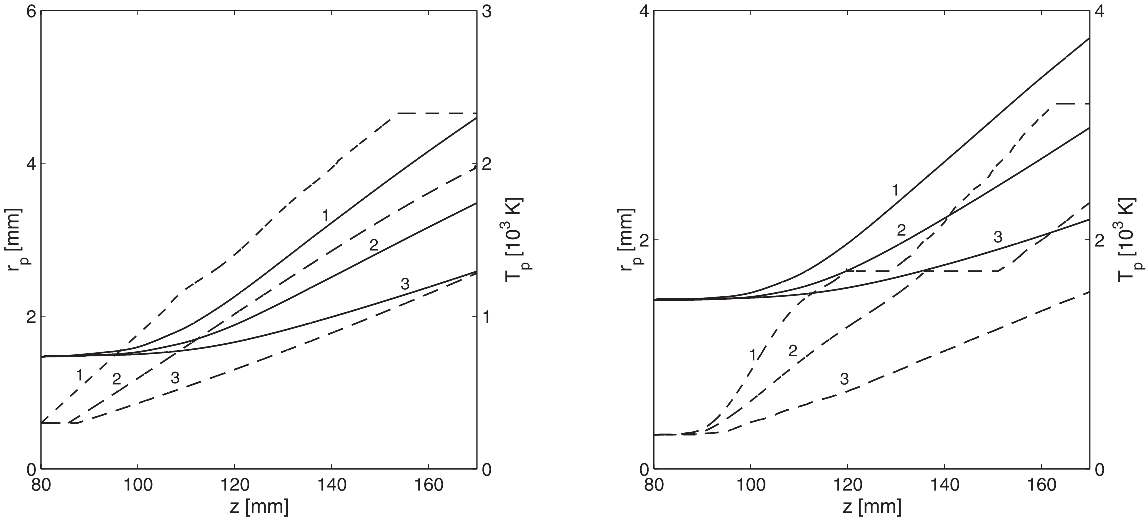

(a) (b)

Fig. 4. Radial position (—) and temperature (- -) of the particles as function of the axial position for (a) `CASE A` (Al_2O_3 particles with $d_{p1,2,3} = 30$, 50, 100 μm and injection point: $x_{inj} = -0.1$ mm $y_{inj} = 1.5$ mm); (b) `CASE B` (Ni particles with $d_{p1,2,3} = 30$, 50, 100 μm and injection point: $x_{inj} = -0.1$ mm, $y_{inj} = 1.5$ mm).

stream as numbered in Figure 2; injection coordinates on the probe exit section will be given in detail in each figure caption. All the figures showing results in terms of particle temperature, T_p, and particle radial position along its trajectory, r_p, as function of the axial coordinate, z, will refer, case by case, to the injection stream for which particles are characterized by the maximum value of radial displacement from the axis at the exit of the torch.

Figures 3a and 3b show the behaviour of Al_2O_3 (injection stream 14 in Fig. 2) and Ni particles (injection stream 27 in Fig. 2), respectively, under the same operating conditions. In both cases, for increasing particle diameters, a decrease in particle temperature and velocity at the torch exit are evidenced as a consequence of an increase in thermal and dynamical inertia. Moreover, only nickel particles with $d_{p1} = 30$ μm can be melted within the discharge, while this occurs also to alumina particles with a diameter equal to 50 μm (with a plateau which is wider than the one for alumina particles with $d_{p1} = 30$ μm). Nickel particles velocity at the exit of the torch appears to be bigger than the one for alumina for $d_{p1,2} = 30{-}50$ μm, while the opposite situation occurs for $d_{p3} = 100$ μm.

Figure 4 show some results with the same operating conditions and materials of Figure 3 and where alumina

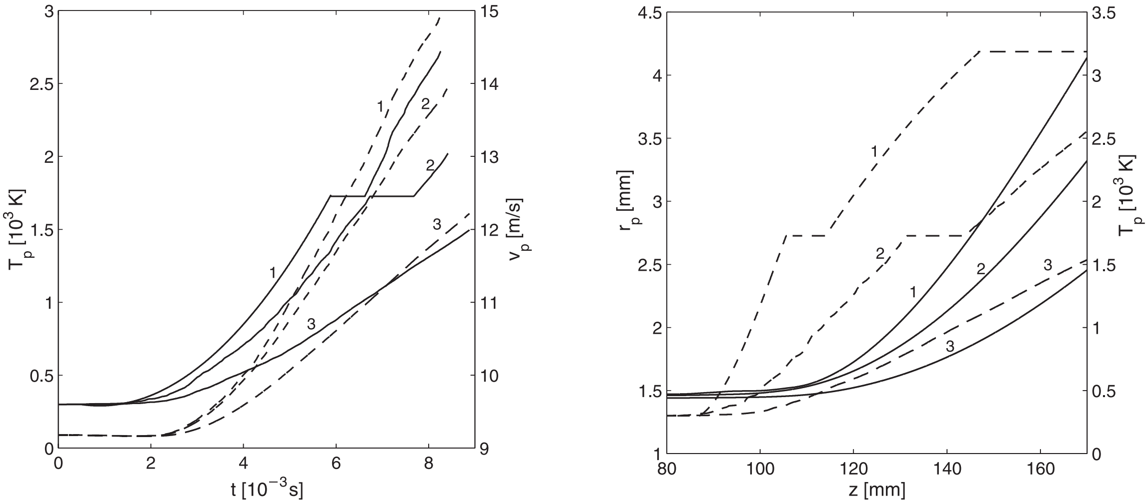

(a) (b)

Fig. 5. `CASE C` (Ni particles): (a) temperature (—) and velocity (- -) of the particles as function of time ($d_{p1,2,3} = 30$, 50, 100 μm; injection point $x_{inj} = 0.2$ mm, $y_{inj} = -0.8$ mm); (b) radial position (—) and temperature (- -) of the particles as function of the axial position ($d_{p1,2,3} = 30$, 50, 100 μm; injection points: $x_{inj} = -0.1$ mm, $y_{inj} = 1.5$ mm for particles with diameter d_{p1}; $x_{inj} = 0.6$ mm, $y_{inj} = 1.3$ mm for particles with diameter d_{p2}; $x_{inj} = 1.2$ mm, $y_{inj} = 0.8$ mm for particles with diameter d_{p3}).

(Fig. 4a) and nickel (Fig. 4b) particles are injected in the same stream (number 4, in Fig. 2). Nickel particles with $d_{p1} = 30$ μm can this time undergo both melting and then evaporation before exiting the torch. For increasing particle size, both materials show a decrease in the radial position of the particle at the exit of the torch with values for alumina always bigger than the corresponding nickel ones.

Figure 5 shows results for nickel particles under operating conditions `C` of Table 3, namely with a plasma gas swirl component of 20 m/s. Figure 5a can be usefully compared with Figure 3b referring to the same injection stream (number 27 in Fig. 2): slight changes appear for what concerns the behaviour of T_p and v_p as function of residence time. Figure 5b shows values of r_p and T_p as function of the axial coordinate for three different particle size and injection points (number 4, 16 and 22 for $d_{p1,2,3} = 30$, 50, 100 μm, respectively); values of r_p at the exit of the torch for particles of 30 μm is slightly bigger than the corresponding ones of Figure 4b, probably due to stronger centrifugal forces induced by the swirl component of the plasma gas. Once again, only particles with $d_{p1} = 30$ μm can undergo both melting and evaporation; in this flow configuration they both occur for smaller values of the axial coordinate with respect to the corresponding cases of Figure 4b.

Figure 6 shows again results for nickel particles injected in the discharge under operating conditions `D` of Table 3, namely with a sheath gas swirl component of 20 m/s. Figure 6a can be usefully compared with Figure 3b since results refer to the same injection stream (number 27 in Fig. 2): only a slight change in particle temperature and velocity behaviour as function of time can be evidenced due to the modified sheath gas conditions of case `D` with respect to `B`. Moreover, no evaporation occurs to nickel particles injected through the stream numbered 27 (see Fig. 2). On the contrary, Figure 6b shows that nickel particles with $d_{p1,2} = 30,\ 50$ μm (injection stream 3 and 1, respectively, in Fig. 2) undergo both melting and evaporation, while for $d_{p3} = 100$ μm only melting occurs in the exit section of the torch. Most important is the effect of the sheath gas swirl component on the radial displacement of particles from the axis at the exit of the torch, which appear from Figure 6b to be much bigger ($r_p \backsim 2.5 \div 8$ mm) then previously evidenced in Figures 4b and 5b (for injection streams that are all located in the external ring of the injection probe).

Figure 7 shows the results for injection of nickel particles in a discharge whose operating conditions differ from the ones of Figure 6 only for an increase in generator frequency up to $f = 5$ MHz (`CASE E` in Tab. 3). Conclusions can be readily drawn on the effect of frequency on the behaviour of T_p and v_p as function of time comparing curves of Figure 7a with the ones of Figure 6a, both referring to injection stream 27: the same behaviour is shown, with only a slight but perceivable time delay for phenomena depicted in Figure 7a with respect to Figure 6a. A most interesting effect that should be mainly due to the three-dimensionality of the phenomena is perceivable comparing Figure 7b with Figure 6b: in fact, while the behaviour of particles with $d_{p1} = 30$ μm (injection stream number 5) at $f = 5$ MHz is very similar (except for a slight time delay) to that of curve 1 in Figure 6b (with injection stream number 3, close to 5, according to Fig. 2), curves 2 and 3 of Figure 7b (referring to injection stream number 24) are quite different from the corresponding ones in Figure 6b

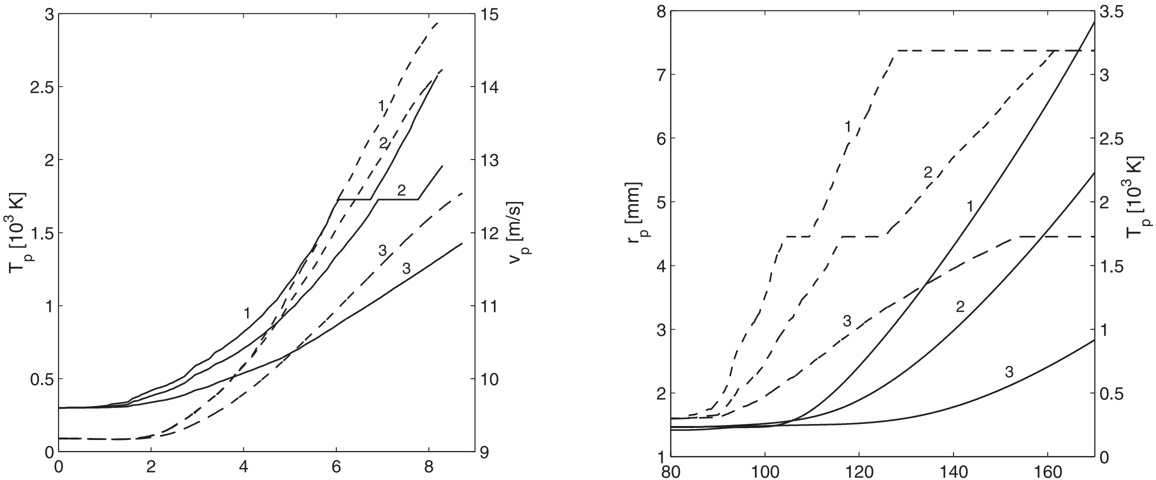

(a) (b)

Fig. 6. `CASE D` (Ni particles): (a) temperature (—) and velocity (- -) of the particles as function of time ($d_{p1,2,3}$ = 30, 50, 100 μm; injection point: $x_{inj} = 0.2$ mm, $y_{inj} = -0.8$ mm); (b) radial position (—) and temperature (- -) of the particles as functions of the axial position ($d_{p1,2,3}$ = 30, 50, 100 μm; injection points: $x_{inj} = -1.1$ mm, $y_{inj} = 0.9$ mm for particles with diameter d_{p1}; $x_{inj} = -1.4$ mm, $y_{inj} = 0.2$ mm for particles with diameters d_{p2} and d_{p3}).

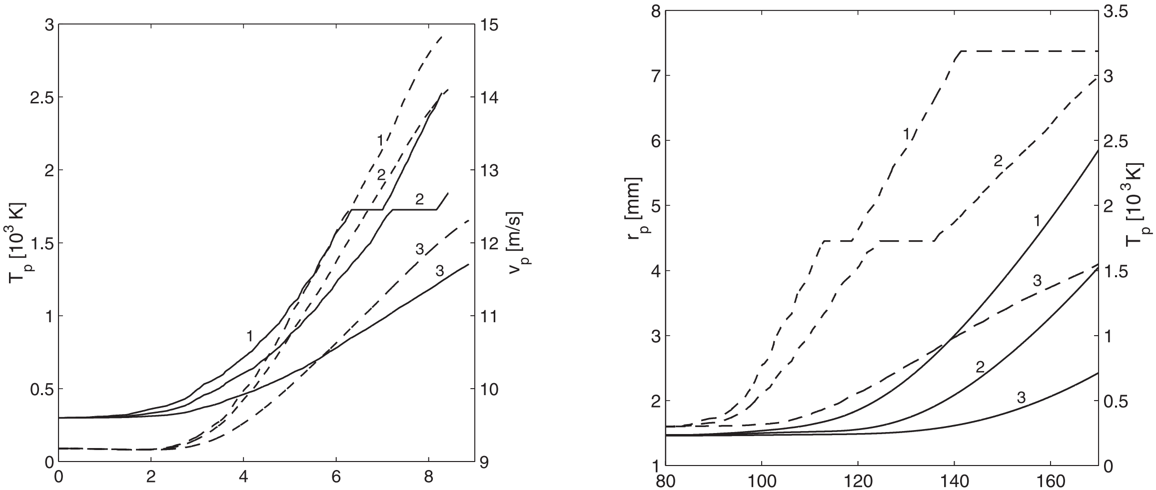

(a) (b)

Fig. 7. `CASE E` (Ni particles): (a) temperature (—) and velocity (- -) of the particles as function of time ($d_{p1,2,3}$ = 30, 50, 100 μm; injection point: $x_{inj} = 0.2$ mm, $y_{inj} = -0.8$ mm); (b) radial position (—) and temperature (- -) of the particles as functions of the axial position ($d_{p1,2,3}$ = 30, 50, 100 μm; injection points: $x_{inj} = -1.4$ mm, $y_{inj} = -0.3$ mm for particles with diameters d_{p1} and d_{p2}; $x_{inj} = 0$ mm, $y_{inj} = -1.5$ mm for particles with diameter d_{p3}).

(referring to injection point number 1): this is probably due to the difference in position for the injection streams. Moreover, Figure 7b shows an effect of reduced values of r_p at the exit of the torch for all the three particle size here considered.

Figures 8 and 9 show results for alumina and nickel particles, respectively, under operating conditions of reduced net power dissipated in the discharge (P = 15 kW) and reduced sheath gas swirl velocity ($v_{\theta s}$ = 10 m/s) at f = 3 MHz. Most evident is the fact that alumina particles do not reach a complete melting (Fig. 8a, injection stream 38) even for the smallest size d_{p1} = 30 μm, while nickel ones coming from the same injection point do (Fig. 9b, curve 1). Melting occurs for nickel particles injected in stream 27 (Fig. 9a, curves 1 and 2) and in streams 38 and 36 (Fig. 9b, curves 1 and 2, respectively); no melting occurs for bigger particles with d_{p3} = 100 μm (Figs. 9a and 9b, curve 3). One more three-dimensional effect can be evidenced comparing temperature histories of nickel particles injected in stream 27 with $d_{p2,3}$ = 50,

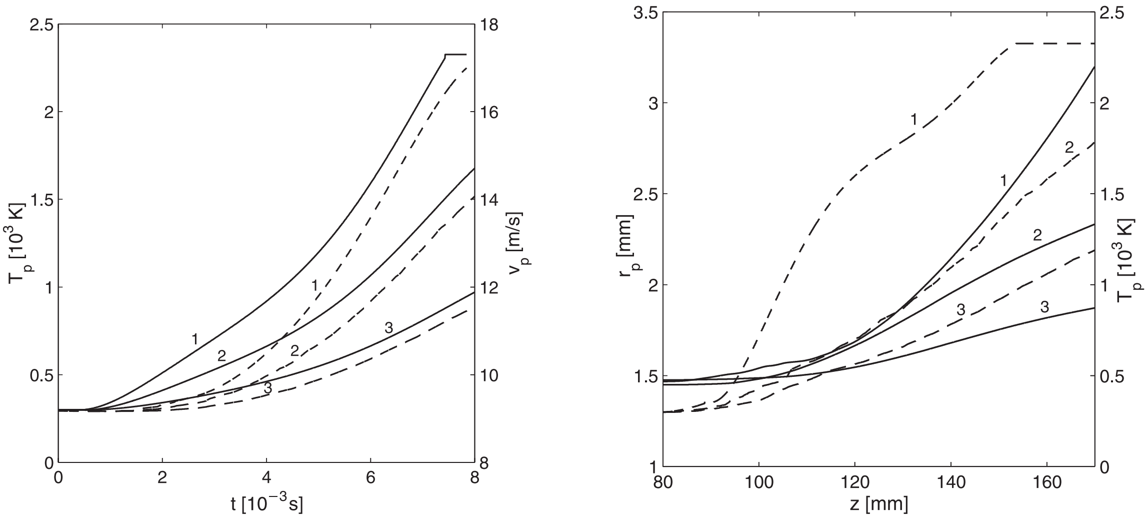

(a) (b)

Fig. 8. `CASE F` (Al_2O_3 particles): (a) temperature (—) and velocity (- -) of the particles as function of time ($d_{p1,2,3}$ = 30, 50, 100 μm; injection point: x_{inj} = 1.1 mm, y_{inj} = −1.0 mm); (b) radial position (—) and temperature (- -) of the particles as functions of the axial position ($d_{p1,2,3}$ = 30, 50, 100 μm; injection points: x_{inj} = −0.6 mm, y_{inj} = 1.4 mm for particles with diameter d_{p1}; x_{inj} = 1.1 mm, y_{inj} = −1.0 mm for particles with diameters d_{p2}; x_{inj} = 1.4 mm, y_{inj} = −0.3 mm for particles with diameter d_{p3}).

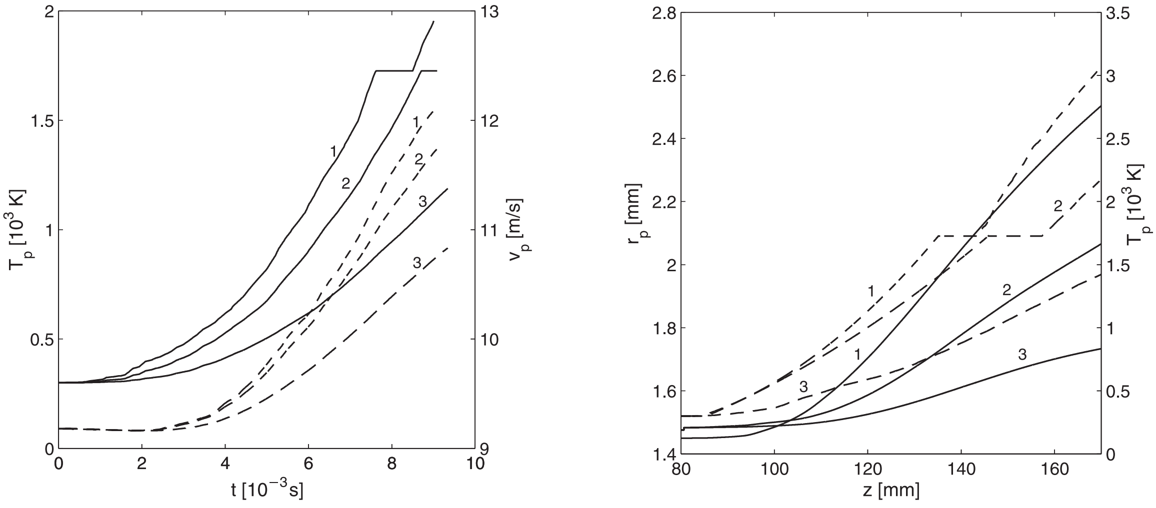

(a) (b)

Fig. 9. `CASE G` (Ni particles): (a) temperature (—) and velocity (- -) of the particles as function of time ($d_{p1,2,3}$ = 30, 50, 100 μm; injection point: x_{inj} = 0.2 mm, y_{inj} = −0.8 mm); (b) radial position (—) and temperature (- -) of the particles as functions of the axial position ($d_{p1,2,3}$ = 30, 50, 100 μm; injection points: x_{inj} = 1.1 mm, y_{inj} = −1.0 mm for particles with diameter d_{p1}; x_{inj} = 1.4 mm, y_{inj} = −0.3 mm for particles with diameters d_{p2} and d_{p3}).

100 μm (Fig. 9a) and the ones injected in stream 36, again with $d_{p2,3}$ = 50, 100 μm (Fig. 9b).

Finally, some results in the previously described framework of presentation refer to injection of tungsten particles (operating condition `H`) at P = 25 kW, f = 3 MHz and axial injection of both plasma and sheath gas. Figure 10a shows the behaviour of T_p and r_p as function of time for tungsten particles injected in stream 37. Complete melting occurs for $d_{p1,2}$ = 30, 50 μm while it must be noticed that particle temperature at the exit of the torch reaches values which are much higher than what previously evidenced for alumina and nickel particles in the whole range of operating conditions for which results have been presented. Figure 10b shows how a complete melting can be achieved for particles with $d_{p1,2}$ = 30, 50 μm also for the injection point 4.

For a test case, a comparison of the plasma temperature fields in the presence and absence of particle injection is made and the results are given in Figures 11 and 12. The torch operating conditions, the gas flow rates

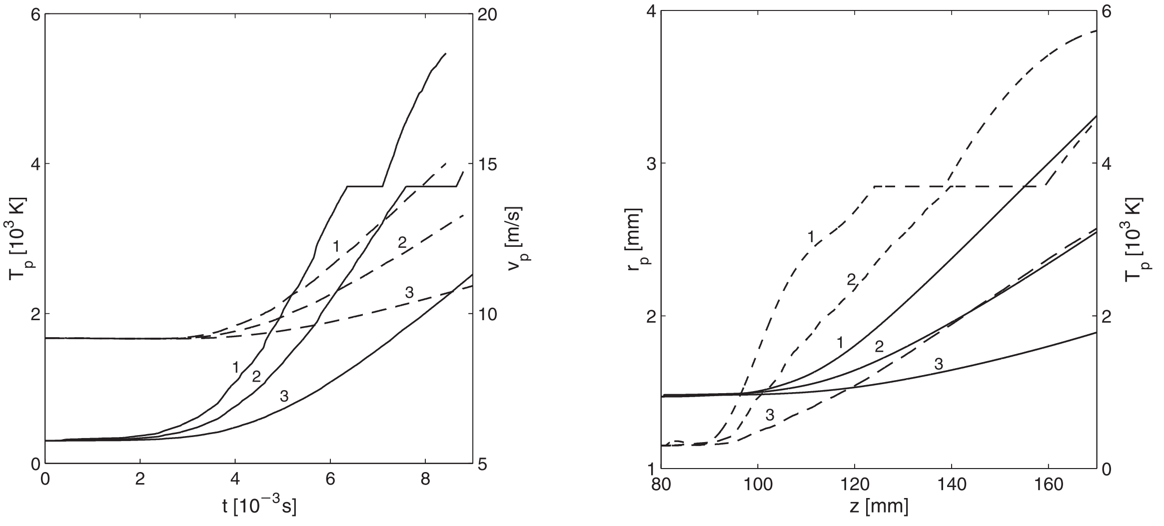

(a) (b)

Fig. 10. `CASE H` (W particles): (a) temperature (—) and velocity (- -) of the particles as function of time ($d_{p1,2,3}$ = 30, 50, 100 μm; injection point: x_{inj} = 1.1 mm, y_{inj} = −0.6 mm); (b) radial position (—) and temperature (- -) of the particles as function of the axial position ($d_{p1,2,3}$ = 30, 50, 100 μm; injection point: x_{inj} = −0.1 mm, y_{inj} = 1.5 mm).

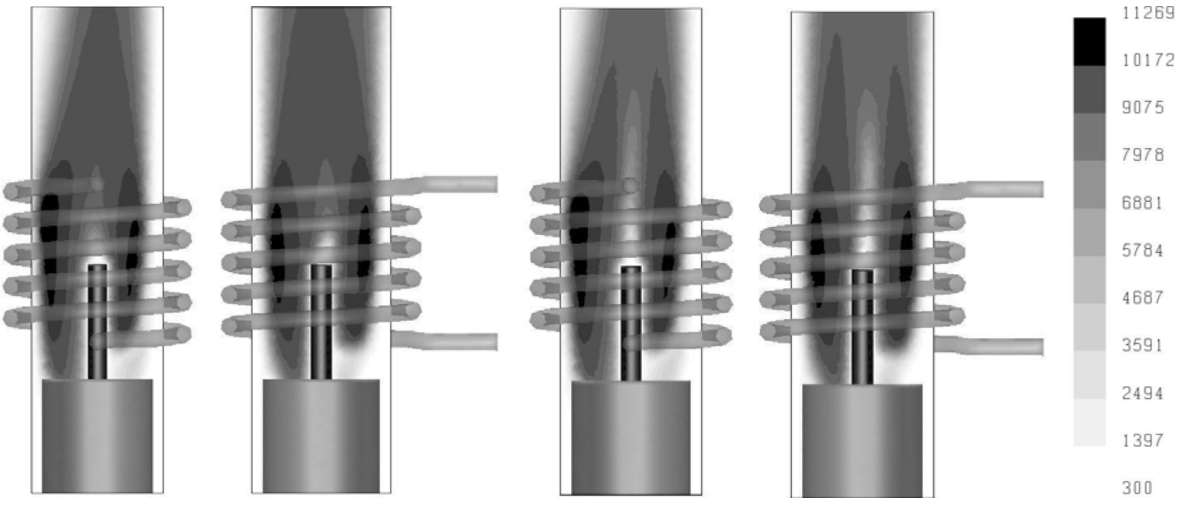

(a) (b) (c) (d)

Fig. 11. Plasma temperature fields [K] on two planes passing through the axis of the torch, whose relative position is evidenced by coil view, for the case without powder injection (a, b) and with powder injection (c, d). The torch operating conditions, gas flow rates and particle material are those of `CASE H`, but with carrier gas flow rate Q_1 = 1 slpm.

and the material of the injected particles (tungsten, with d_{p1} = 30 μm) are those of `CASE H`, except for what concerns the carrier gas flow rate, Q_1, which is assumed to be equal to 1 slpm. Figures 11a and 11b show the plasma temperature fields on two vertical, perpendicular, planes passing through the axis of the torch, for the case without powders injection; Figures 11c and 11d show, with the same type of visualization, plasma temperature fields given for the case with particles injection.

Figure 11 clearly states that the overall effect of particle injection in the plasma is a three-dimensional one for what concerns plasma temperature (and plasma flow) fields.

For what concerns the three-dimensionality of the behaviour of trajectories and thermal histories of the particles, conclusions can be drawn from the results presented in Figure 12. Particle temperature and its radial position is shown as function of the curvilinear coordinate, s, along the trajectory for the same selected injection streams (number 1, 4, 5 according to Fig. 2). Time elapsed from the injection ($t = 0$) are as well reported, giving additional information on the residence time of the particles in the discharge.

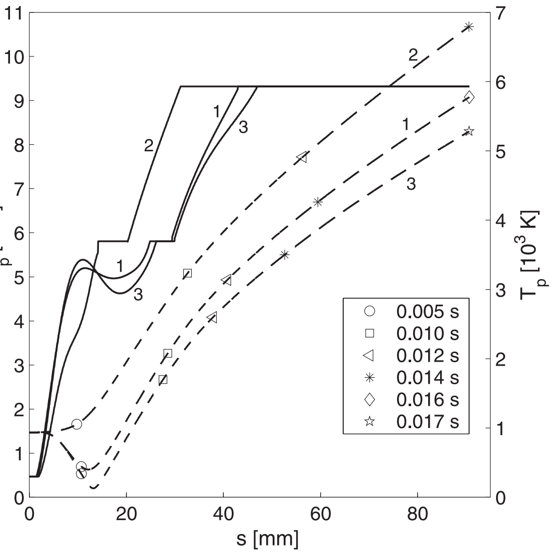

Fig. 12. Time evolution of temperature (—) and radial position (- -) of the W particles as function of the curvilinear coordinate s along their trajectories for three injection streams: curve 1 (injection point: $x_{inj} = -1.4$ mm, $y_{inj} = 0.2$ mm), curve 2 (injection point: $x_{inj} = -0.1$ mm, $y_{inj} = 1.5$ mm), curve 3 (injection point: $x_{inj} = -1.4$ mm, $y_{inj} = -0.3$ mm). Operating conditions as in Figure 11.

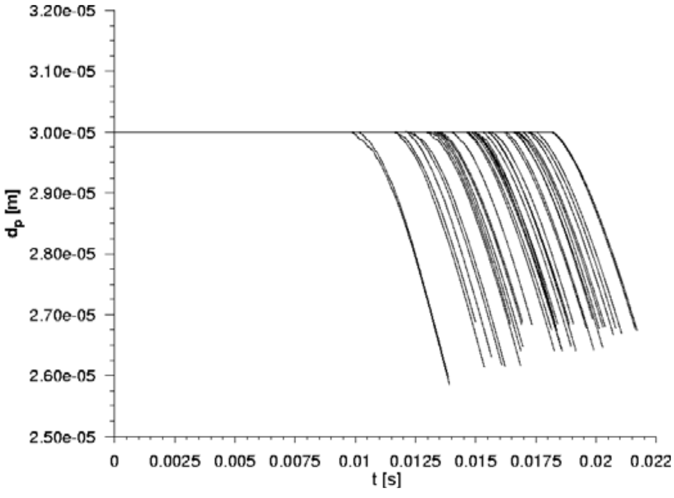

Fig. 13. Time evolution of W particle diameters from the injection point to the exit of the torch. Operating conditions as in Figure 11.

Figure 13 shows the time evolution of tungsten particle diameters tracked from the injection point up to the exit of the torch, while Figure 14 describes, within the limit of a non-stochastic treatment of particle injection, the distribution of their velocities at the exit of the torch. Figure 15, for the same case and operating conditions of Figures 11–14, shows a prediction of the dispersion of tungsten particles within the discharge at four successive sections of the torch, including the injection one, evidencing once again the three-dimensionality of the phenomena under study.

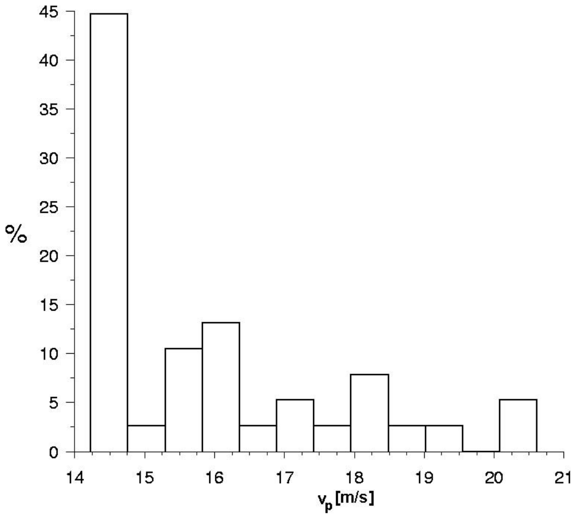

Fig. 14. Histogram for W particle velocities at the exit of the torch. Operating conditions as in Figure 11.

Figure 16 shows a 3–D schematic of nickel particle trajectories within the discharge under operating conditions as those of `CASE D` but with Q_1 equal to 0.5 slpm. A reduced value of Q_1 has been suitably chosen to avoid the central channeling of injected particles and to highlight, strictly for test simulation purposes, a 3–D effect which in a real technological configuration would be highly undesirable.

4 Conclusions and future developments

In this paper, a first step in the modelling of the injection of spherical particles into ICPTs working at atmospheric pressure is presented, in the frame of a fully-coupled model which takes into account the trajectories and temperature histories of the particles under plasma conditions, and a selection of the simulation results is shown, with the limited final aim of putting into evidence how 3–D modelling of the ICPT device could be usefully employed to predict particle behaviour in a wide range of operating conditions. 3–D effects on particle trajectories, their heating histories and plasma flow and temperature fields are shown to be appreciable. These results have been obtained for an LTE argon plasma in laminar flow and for three types of particles (Al_2O_3, Ni and W) of fixed diameters (equal to 30, 50 or 100 μm). The particles have been assumed to be injected in the discharge region by means of an idealized probe which delivers them axially through a limited number of streams and perpendicularly to the exit section of the probe, with velocity and temperature equal to those of the carrier gas. The flow field is assumed to be affected only through local plasma temperature changes. Changes in the thermodynamical and transport properties of the plasma due to particle evaporation has not been taken into account.

Future efforts will be devoted to improve the developed model by means of a more realistic simulation of the

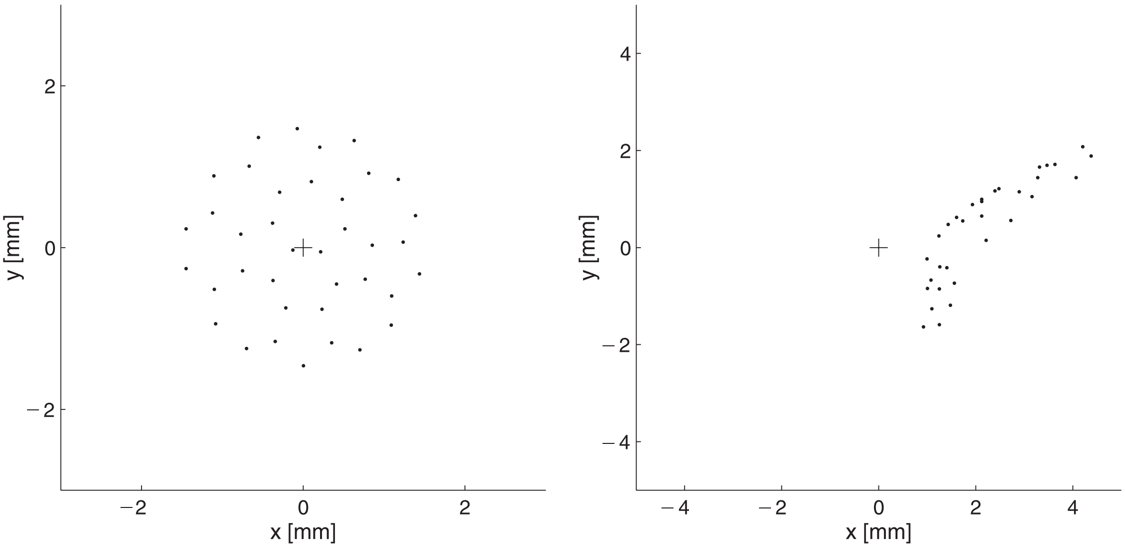

(a) $z = z_{inj} = 80$ mm (b) $z = 110$ mm

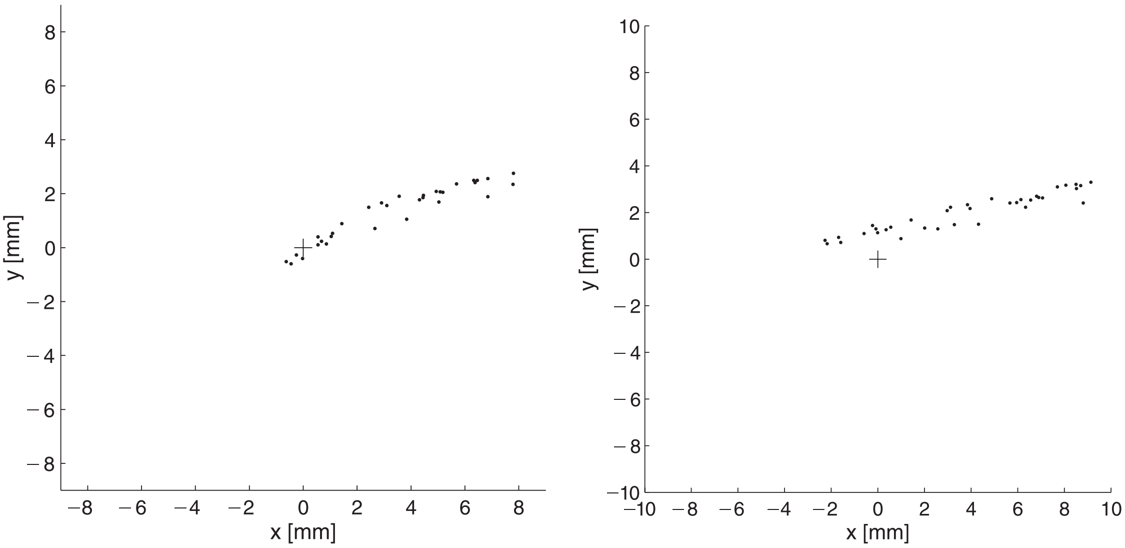

(c) $z = 140$ mm (d) $z = z_{exit} = 170$ mm

Fig. 15. Comparison of the predicted dispersed W particle distributions at four successive sections of the torch. Operating conditions as in Figure 11.

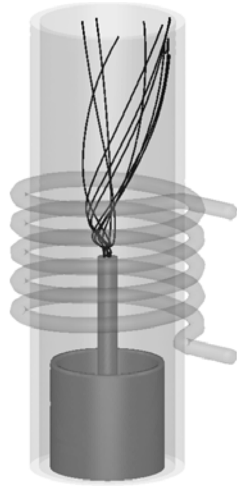

Fig. 16. 3–D schematic of Ni particle trajectories for torch operating conditions where gas flow rates and particle material are those of `CASE D`, but with carrier gas flow rate $Q_1 = 0.5$ slpm.

injection of particles in the torch, taking into account a Gaussian particle size distribution and a randomly distributed direction of injection, which has not yet been attempted in this 3–D framework: a wider parametric study should be performed to deeply investigate the effect of changing the main torch operating conditions (such as carrier gas flow rate, Q_1, and the mass feed rate of the particles, which throughout the present study has been assumed to be equal to 20 g/min). Further improvements also need to be made in order to be able to simulate the injection of particles into a $\mathrm{Ar-H_2}$ gas mixture and to account for torch configurations where turbulent phenomena might be important.

This work was performed with partial financial support from the University of Bologna Goal-Oriented project 2001–2003 and ex-60% 2001–2002 projects, from the Italian Ministry of Education, University and Scientific Research (MIUR) national project COFIN2002 and National Group for Mathematical Physics (GNFM) of the Italian Institute of High Mathematics.

References

1. N.M. Dignard, M.I. Boulos, Metallic and Ceramic Powder Spheroidization by Induction Plasmas, *Int. Thermal Spray Conf. (ITSC-98)*, Nice, France, 1998
2. P. Proulx, J. Mostaghimi, M.I. Boulos, Int. J. Heat Mass Trans. **28**, 1327 (1985)
3. P. Proulx, J. Mostaghimi, M.I. Boulos, Plasma Chem. Plasma Process. **7**, 29 (1987)
4. H. Li, X. Chen, Plasma Chem. Plasma Process. **22**, 27 (2002)
5. D.-Y. Xu, X. Chen, K. Cheng, J. Appl. Phys. **36**, 1583 (2003)
6. D. Bernardi, V. Colombo, E. Ghedini, A. Mentrelli, T. Trombetti, Powders Trajectory and Thermal History Within 3-D Modelling of Inductively Coupled Plasma Torches, *Proceedings of the IV International Conference Plasma Physics and Plasma Technology (PPPT–4)*, Minsk, Belarus, 15–19 September 2003, Vol. 2, pp. 463–464
7. D. Bernardi, V. Colombo, E. Ghedini, A. Mentrelli, T. Trombetti, Powders Trajectory and Thermal History within 3-D ICPTs Modelling for Spheroidization and Purification Purposes, *Proceedings of the 48 Internationales Wissenschaftliches Kolloquium (48.IWK)*, Ilmenau, Deutschland, 22–25 September 2003, pp. 285–286, paper `07_03_04` on CD-ROM (2003)
8. D. Bernardi, V. Colombo, E. Ghedini, A. Mentrelli, T. Trombetti, 3–D Numerical Simulation of Fully-Coupled Particle Heating in ICPTs, *Proceedings of the 4th International Conference on Electromagnetic Processing of Materials (EPM2003)*, Lyon, France, 14–17 October 2003
9. D. Bernardi, V. Colombo, E. Ghedini, A. Mentrelli, T. Trombetti, 3–D Numerical Study of Particle Behavior in ICPTs, *56th Gaseous Electronics Conference (GEC03)*, San Fancisco, CA, USA, 21–24 October 2003
10. D. Bernardi, V. Colombo, E. Ghedini, A. Mentrelli, Eur. Phys. J. D **22**, 119 (2003)
11. D. Bernardi, V. Colombo, E. Ghedini, A. Mentrelli, Eur. Phys. J. D **27**, 55 (2003)
12. D. Bernardi, V. Colombo, E. Ghedini, A. Mentrelli, Three dimensional modelling of inductively coupled plasma torches, *Proceedings of the 16th International Symposium on Plasma Chemistry (ISPC-16)*, Taormina, Italy (2003), paper `ISPC-634` on CD-ROM; Pure Appl. Chem. (in publication as invited contribution, 2004)
13. D. Bernardi, V. Colombo, E. Ghedini, A. Mentrelli, Eur. Phys. J. D **25**, 271 (2003)
14. D. Bernardi, V. Colombo, E. Ghedini, A. Mentrelli, Eur. Phys. J. D **25**, 279 (2003)
15. FLUENT 6.1 User's Guide (Junuary 28, 2003), FLUENT Inc., Chapter 21: Discrete Phase Models, pp. 68–71
16. M.I. Boulos, Pure Appl. Chem. **57**(9), 1321 (1985)
17. P.C. Huang, J. Heberlein, E. Pfender, Surf. Coat. Tech. **73**, 142 (1995)